Nanoscale Advances

ROYAL SOCIETY OF CHEMISTRY

PAPER

View Article Online
View Journal | View Issue

Cite this: *Nanoscale Adv.*, 2025, **7**, 7363

DFT investigation of dye adsorption on pristine and doped graphdiyne: toward efficient removal of disperse yellow 3 from wastewater

Mohamed M. Aboelnga, †*[ab] Mariam M. Seliem, †[a] Elsayed El-Bayoumy [a] and Mohsen El-Tahawy *[c]

The persistence of industrial dyes such as Disperse Yellow 3 (DY3) dye in wastewater remains an environmental concern due to their chemical stability and toxicity. Graphdiyne (GDY), a two-dimensional (2D) carbon-based material, offers a promising platform for adsorption owing to its porous structure and extended π-conjugation. However, its pristine-GDY form exhibits limited binding performance. To enhance its interaction with pollutants, silicon (Si) and germanium (Ge) doping were introduced. This study employs Density Functional Theory (DFT) to examine the adsorption behavior of DY3 dye on pristine, Si-doped, and Ge-doped GDY under both vacuum and aqueous conditions. Four optimized configurations which are parallel, side-parallel, carbonyl-linked, and carbon-linked were analyzed in both pristine and doped models. The results show minimal changes in adsorption energy and geometry in water, confirming the structural integrity of the systems under realistic conditions. Electronic structure analyses including Density of States (DOS), the Natural Bond Orbital (NBO), molecular orbital studies (HOMO–LUMO), infrared (IR) and Reduced Density Gradient–Non-Covalent Interaction (RDG–NCI) visualizations reveal enhanced charge transfer, reduced energy gaps, and distinguishable physisorption and chemisorption features upon doping. Among all models, Si-GDY in the carbonyl-linked configuration exhibits the highest binding energy (−6.00 eV), indicating its superior stability. Additionally, thermodynamic parameters were calculated, revealing improved adsorption performance in doped systems. Non-covalent interaction analysis further confirmed the role of electrostatic, electronic, and charge transfer interactions in stabilizing dye adsorption. These findings demonstrate that doped GDY, particularly Si-GDY, offers enhanced adsorption efficiency, making it a promising candidate for environmental remediation involving persistent dye pollutants.

Received 28th July 2025
Accepted 21st September 2025

DOI: 10.1039/d5na00720h

rsc.li/nanoscale-advances

1. Introduction

The removal of contaminants from industrial wastewater is a critical environmental concern. Dyes, widely used in the textile, leather, food, cosmetics, and paper industries, are among the top three pollutants, with over 700 000 tons consumed annually.[1–3] These pollutants are mutagenic, carcinogenic, and harmful to aquatic ecosystems.[4,5] DY3 dye is one of the most widely used for dyeing synthetic fibers due to its conjugated molecular structure that provides excellent thermal and photostability, while its low water solubility necessitates the use of dispersing agents for effective application.[6] It is extensively used in the textile industry to impart bright, long-lasting coloration to materials such as polyester.[7] However, exposure to its powdered form can lead to skin, eye, and respiratory irritation. Moreover, animal studies have indicated potential genotoxic and carcinogenic effects, although human evidence remains inconclusive.[8] Furthermore, improper disposal of DY3 dye may cause environmental contamination that adversely affects aquatic ecosystems, highlighting the need for stringent safety and waste management protocols.[9] Various removal technologies exist, including filtration, chemical precipitation, ion exchange, adsorption, electrodeposition, and membrane processes.[5,10,11] Among these, adsorption is preferred due to its low cost, simplicity, and efficiency in removing toxic pollutants.[10,12] Adsorption is an effective method for removing dyes from wastewater due to its ability to capture pollutants efficiently. It relies on the interaction between dye molecules and adsorbent surfaces, making it a promising approach for environmental remediation.[10,12]

[a]*Chemistry Department, Faculty of Science, Damietta University, 34511 Damietta, Egypt. E-mail: mohamed-aboelnga@du.edu.eg; students.du.edu.eg; sayedelbayoumy@du.edu.eg*

[b]*King Salman International University, Faculty of Science, Ras Sudr, 46612, South Sinai, Egypt*

[c]*Chemistry Department, Faculty of Science, Damanhour University, 22511, Damanhour, Egypt. E-mail: mohsen.eltahawy@sci.dmu.edu.eg*

† Contributed equally to this work.

Various adsorbents have been extensively used including activated carbon,[13] zeolites,[14] polymeric adsorbents,[15] metal–organic frameworks (MOFs),[16] and graphene-based materials.[17] GDY, a new carbon allotrope, was used as an adsorbent for wastewater treatment due to its unique 2D porous network that yields an exceptionally high surface area and abundant active sites.[18] It has a highly π-conjugated structure, making it promising for applications in gas separation, catalysis, water remediation, sensors, and energy storage.[19–26] GDY is typically synthesized *via* chemical vapor deposition (CVD) on metal substrates followed by controlled thermal treatment to form its well-ordered framework.[27,28] It features a network of benzene rings interconnected by triple (–C≡C–) bonds, providing excellent electronic and chemical properties.[29]

Doping has proven to be a pivotal strategy in tailoring the structural and electronic properties of two-dimensional materials, thereby enhancing their adsorption and sensing capabilities. For instance, Mg doping in amorphous ZnO nanoparticles has been shown to reduce the bandgap and modify optical properties, leading to improved performance in various applications.[30] Similarly, Zn doping in $CuLaSe_2$ quantum dots has been observed to influence photoluminescence behavior, indicating alterations in the electronic structure conducive to sensing applications.[31] These studies underscore the role of atomic-scale functionalization in modulating material properties, providing a rationale for exploring doping effects in GDY-based systems. To enhance the stability of the systems and tailor the electronic properties of GDY, doping with heteroatoms such as silicon and germanium is introduced as a strategic approach. Doping not only modifies the local electronic structure of GDY but also enhances its surface reactivity, facilitates charge transfer interactions, and creates active sites for stronger adsorption. Similar strategies have been reported for doping other carbon-based nanostructures to improve adsorption and reactivity.[32–36] These modifications are expected to improve the efficiency, sensitivity, and specificity of dye removal and sensing processes.[37–39] A dopant, owing to its abundance and unique properties, plays a crucial role in enhancing the thermal and mechanical stability of GDY.[40–42] Silicon also enhances optical behavior by modifying the band gap, making GDY more sensitive to photoreactions, which is important in applications relying on light absorption and chemical catalysis. Additionally, silicon doping generates additional binding sites for metal centers, increasing the capacity to interact with molecules like dyes or pollutants,[43–49] and this behavior is consistent with findings from previous DFT studies on doped nanomaterials.[50–53] Furthermore, germanium, similar in chemical structure to silicon but with a larger atomic mass, offers different effects on the surface and electronic properties of GDY. Germanium doping enhances surface activity and increases the efficiency of chemical reactions by increasing electron density in surrounding areas, which improves adsorption of dyes such as DY3. Germanium also plays a vital role in enhancing electrical conductivity, which is essential in electronic and sensing applications.[54,55] Similar effects have been explored in computational sensing studies involving Ge-functionalized surfaces.[55–57]

In this study, DFT is employed to explore and compare the adsorption behavior of DY3 dye on pristine GDY, silicon-doped GDY (Si-GDY), and germanium-doped GDY (Ge-GDY). Multiple adsorption configurations which are parallel, side-parallel, carbonyl-linked, and carbon-linked are optimized and analyzed. To better understand the underlying adsorption mechanisms, advanced computational tools are utilized, including DOS, IR spectroscopy, RDG–NCI analysis, HOMO–LUMO and NBO analysis. Previous theoretical studies have also used similar approaches to investigate adsorption processes.[56,58,59] Further insight into adsorption-induced modifications was obtained through DOS and IR analysis. DOS revealed energy level shifts, especially the changes in the HOMO–LUMO gap,[60] clarifying charge transfer and adsorption stability.[61] IR spectra highlighted vibrational shifts and intensity changes, indicating bond formation and distinguishing between physisorption and chemisorption.[62] These tools collectively offered a comprehensive view of the interaction dynamics. Additionally, the study evaluates thermodynamic parameters (ΔG, ΔH, and ΔS).[63,64] The results also showed that introducing the water effect into the calculations did not significantly impact the adsorption energies, as the values were very close to those calculated in vacuum. This indicates that the interaction between the DY3 dye and the studied GDY surfaces is strong enough to remain stable even in an aqueous environment, supporting the potential application of these materials in actual environment or water-based systems without loss of adsorption efficiency. By systematically investigating both pristine and doped GDY systems, this research provides valuable insights for the rational design of enhanced adsorbents and functional sensing materials for environmental remediation.

2. Computational methods

DFT calculations were used to investigate the adsorption behavior of DY3 dye onto both pristine and metal-doped GDY surfaces in gaseous and aqueous phases. These calculations allowed for the prediction of adsorption mechanisms through the determination of molecular descriptors and adsorption energies, specifically by evaluating the binding energy between the DY3 dye and GDY. Geometry optimizations and electronic characteristics for all the studied complexes and different binding orientations were performed using the Gaussian 16 software on both pristine GDY and metal-doped GDY,[65] where the system was modeled as a finite molecular cluster.[66,67] The structure of pristine-GDY consists of a carbon-based framework with distinctive benzene rings and acetylenic linkages (–C≡C–C≡C–). GDY is composed of seven benzene rings, six of which are each saturated with three hydrogen atoms, totaling 18 hydrogen atoms. These six benzene rings are interconnected forming a planar network, while the seventh ring connects to five carbon atoms and one silicon or germanium atom, representing a substitutional doping site with a ratio of one silicon or germanium atom per 65 carbon atoms. The system was modeled in a singlet spin state, and the optimized structure represents a finite molecular cluster with approximate

dimensions of 18.06 Å × 17.56 Å × 4.55 Å along the *X*, *Y*, and *Z* axes, respectively. DFT calculations were conducted using the B3LYP hybrid functional, which effectively incorporates both exchange and correlation effects.[68,69] This combination has been successfully employed to represent various chemical systems.[70–72] The standard 6-31G(d) basis set was applied to ensure a suitable balance between computational cost and accuracy. To confirm the reliability of the 6-31G(d) basis set in describing dispersion and charge transfer interactions, selected geometries were re-optimized using the B3LYP-GD3 functional, showing no significant geometric deviations for doping systems. Full computational details are provided in the SI (Fig. S6 on page 8). DFT enabled the identification of potential adsorption sites and predicting non-covalent bonding between GDY and DY3 dye.[73–82] Moreover, environmental effects could be explored using either implicit[83–87] or explicit solvation models in previous studies.[88–93] In this study, all the obtained geometries in vacuum have been re-optimized by accounting for solvent effects implicitly by employing the Integral Equation Formalism Polarizable Continuum Model (IEFPCM), which has been successfully used in similar investigations.[94–97] This approach allowed us to evaluate the influence of the aqueous environment on the adsorption behavior and electronic properties of the DY3 dye on pristine and doped GDY surfaces. Frequency calculations confirmed that all optimized structures correspond to true minima on the potential energy surface, with no imaginary frequencies detected. The molecular structures and the electronic properties, including the highest occupied molecular orbitals (HOMOs) and lowest unoccupied molecular orbitals (LUMOs) have been analyzed and visualized utilizing the GaussView 6.0. To explore non-covalent interactions, visual molecular dynamics (VMD),[98] Gnuplot,[99] and the natural bond orbital (NBO) analysis were performed on the obtained GDY-DY3 dye complexes, employing the same level of theory and basis set,[100] and Multiwfn software[101] was employed for generating RDG plots and NCI iso-surfaces. DOS and IR spectra were analyzed utilizing GaussSum software.[102] The binding energy (E_{bind}) is defined as follows:

$$E_{bind} = E_{GDY\backslash DY3\ dye} - (E_{DY3\ dye} + E_{GDY}) \quad (1)$$

Here, $E_{DY3\text{-}dye}$ represents the energy of the DY3 dye, E_{GDY} is the energy of GDY, and $E_{GDY\backslash DY3\text{-}dye}$ is the energy of the interacting DY3-GDY complex, with different orientations, where the negative adsorption energies indicate that the complexation process is exothermic.

The HOMO–LUMO energy gap (E_{gap}) is estimated from the difference between the HOMO′ energy (E_H) and LUMO energy (E_L),[103] which is expressed as follows:

$$E_{gap} = E_L - E_H \quad (2)$$

where a large E_{gap} signifies chemically hard molecules that interact weakly with other systems, in contrast, a moderate E_{gap} enhances reactivity by facilitating favorable HOMO–LUMO interactions in chemical processes.[104]

3. Results and discussion

Initially, we have explored different optimized binding modes for the adsorption of DY3 dye on pristine, Si-doped, and Ge-doped GDY surfaces, considering various molecular orientations: parallel, side-parallel, carbonyl-linked, and carbon-linked. This investigation has been further expanded using several analytical tools, such as RDG–NCI analysis, DOS, IR spectroscopy, NBO analysis and HOMO–LUMO gap analysis, to gain a comprehensive understanding of molecular interactions and behavior.

3.1. Electronic and spectroscopic analysis for the adsorption of DY3 dye on pristine GDY

To initiate the investigation of DY3 dye adsorption, four optimized configurations on pristine-GDY were examined (see Fig. 1), including the parallel (Fig. 1a), side-parallel (Fig. 1b), carbonyl-linked (Fig. 1c), and carbon-linked (Fig. 1d). Notably, some binding modes observed in pristine GDY were absent in silicon- or germanium-doped GDY systems, highlighting the influence of doping on adsorption patterns. In the parallel-side configuration, the molecule adopts a T-shaped orientation, where one aromatic ring of the molecule is positioned nearly

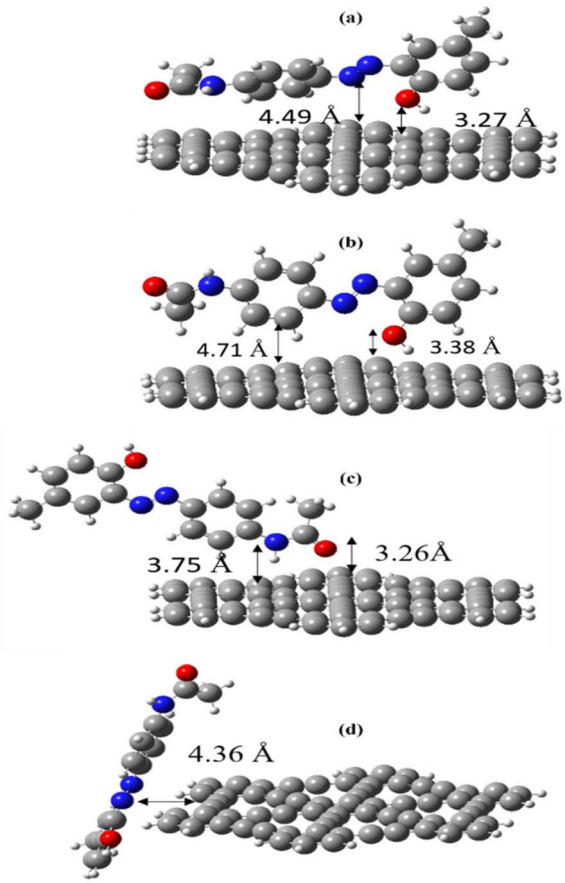

Fig. 1 The four explored orientations of adsorption of DY3 dye on pristine GDY: (a) parallel, (b) parallel-side, (c) carbonyl-linked, and (d) carbon-linked.

perpendicular to the GDY surface, facilitating T-shaped and π–π interactions, with an interatomic distance of about 3.38 Å between the carbon atoms of the perpendicular ring and the GDY surface, suggesting a moderate interaction strength. In the carbonyl-linked configuration, the molecule is linked to the GDY surface *via* its carbonyl group, leading to dipole–dipole interactions. The oxygen atom of the carbonyl group is situated at an interatomic distance of nearly 3.26 Å from the closest carbon atom on the GDY surface, reflecting a relatively strong interaction. The carbon-linked configuration depicts a side-on adsorption, where the molecule is oriented laterally relative to the GDY surface. This setup results in van der Waals interactions with interatomic distances 4.36 Å between the azo group of the molecule and the GDY surface, indicating weaker adsorption compared to the other configurations. Amongst these studied configurations, the parallel configuration (Fig. 1a) is the most favorable in vacuum, exhibiting an adsorption energy of −0.21 eV. This configuration benefits from strong π–π stacking interactions between the aromatic rings of DY3 and the π-conjugated system of GDY. The interatomic distances, nearly 4.49 Å between the azo nitrogen atom and the nearest carbon atom on GDY, and about 3.27 Å between carbonyl carbon and the nearest carbon atom on GDY, indicate a stable adsorption geometry.

Electronic parameters such as the highest occupied molecular orbital energy (E_{HOMO}), lowest unoccupied molecular orbital energy (E_{LUMO}), and energy gap (E_G), alongside other global descriptors, are summarized in Table 1. The HOMO and LUMO in vacuum are illustrated in Fig. S1. The DOS spectra shown in Fig. 2c reveal notable alterations in orbital configurations following DY3 dye adsorption on pristine GDY, indicating significant electronic interactions between the dye and the surface. Complementing this, the IR spectra (Fig. 2d) display shifts in vibrational modes, indicative of chemical bonding rather than mere physical adsorption. Furthermore, the RDG sign(λ_2)ρ plots and NCI isosurfaces presented in Fig. 2a and b confirm the presence of weak to moderate non-covalent interactions, primarily van der Waals forces and π–π stacking that stabilize the adsorption complex. The corresponding analyses for the remaining configurations (side-parallel, carbonyl-linked, and carbon-linked) are provided in Fig. S2, including RDG, NCI, DOS, and IR spectra. The results depicted in Fig. 1 and 2 provide a detailed data of DY3 dye adsorption on pristine GDY, revealing how molecular orientation affects binding modes, electronic structure, and vibrational properties, which are key factors for optimizing GDY-based materials in sensing and optoelectronic applications. To enhance the DY3 dye adsorption efficiency on the surface of GDY, Sections 3.2 and 3.3 will discuss the effects of silicon and germanium doping on the structural and electronic properties of the materials.

3.2. Influence of silicon doping on electronic behavior of the complex

The optimized adsorption configurations of the DY3 dye molecule on the Si-GDY surface are shown in Fig. 3(a–d). The different adsorption configurations of the DY3 dye on the Si-GDY surface are analyzed based on the interatomic distances that range from 1.72 Å to 1.96 Å. The various electronic interactions are also presented. In the (a) configuration, the interaction distance is 1.96 Å, indicating the formation of a covalent bond between the Si atom and the carbon of the DY3 dye. The molecule is nearly perpendicular to the surface. Intermediate adsorption strengths are observed in configuration (b), which shows coordinate covalent bonding with Si, supported by donor–acceptor interactions from the lone pair of the DY3 dye to the vacant orbital of the silicon atom, and the (d) configuration shows covalent bonding. The bonding distances are 1.79 Å and 1.94 Å, respectively, indicating weaker yet significant covalent character compared to configuration (c). In the (c) configuration, the interaction distance is 1.72 Å, indicating strong covalent bonding between the dye and Si atom, the

Table 1 HOMO and LUMO energies (E_{HOMO} and E_{LUMO}), HOMO–LUMO gap (E_G), ionization potential (IP), electron affinity (EA), chemical hardness (η), softness (χ), chemical potential (μ_{ch}), electrophilicity index (ω), and the adsorption energies (E_{ads}) for systems of DY3/GDY, DY3/Si-GDY, and DY3/Ge-GDY with different orientations in vacuum

System	HOMO (eV)	LUMO (eV)	ΔE (eV)	IP (eV)	EA (eV)	η (eV)	χ (eV)$^{-1}$	μ_{ch} (eV)	ω (eV)	$E_{ads.}$ (eV)
Parallel	−5.19	−2.68	−2.51	5.19	2.68	1.25	0.796	−3.93	6.16	−0.21
Side-parallel	−5.25	−2.76	−2.49	5.25	2.76	1.24	0.80	−4.00	6.45	−0.20
Carbon-linked	−5.14	−2.54	−2.60	5.14	2.54	1.30	0.77	−3.84	5.66	−0.15
Carbonyl-linked	−5.13	−2.54	−2.59	5.13	2.54	1.29	0.77	−3.83	5.67	−0.10
Si-GDY										
Parallel	−13.22	−12.94	−0.28	13.22	12.94	0.14	7.26	−13.08	620.47	−4.81
Side-parallel	−13.58	−13.09	−0.48	13.58	13.09	0.24	4.13	−13.33	367.11	−5.28
Carbon-linked	−13.31	−12.83	−0.48	13.31	12.83	0.24	4.19	−13.07	358.59	−5.91
Carbonyl-linked	−12.71	−12.51	−0.20	12.71	12.51	0.10	10.24	−12.61	813.76	−6.00
Ge-GDY										
Parallel	−13.66	−13.18	−0.48	13.66	13.18	0.24	4.14	−13.42	372.31	−4.49
Side-parallel	−13.58	−13.11	−0.47	13.58	13.11	0.24	4.24	−13.35	377.25	−5.01
Carbon-linked	−13.28	−12.82	−0.46	13.28	12.82	0.23	4.34	−13.05	369.45	−5.68
Carbonyl-linked	−12.71	−12.52	−0.19	12.71	12.52	0.10	10.51	−12.61	836.52	−5.35

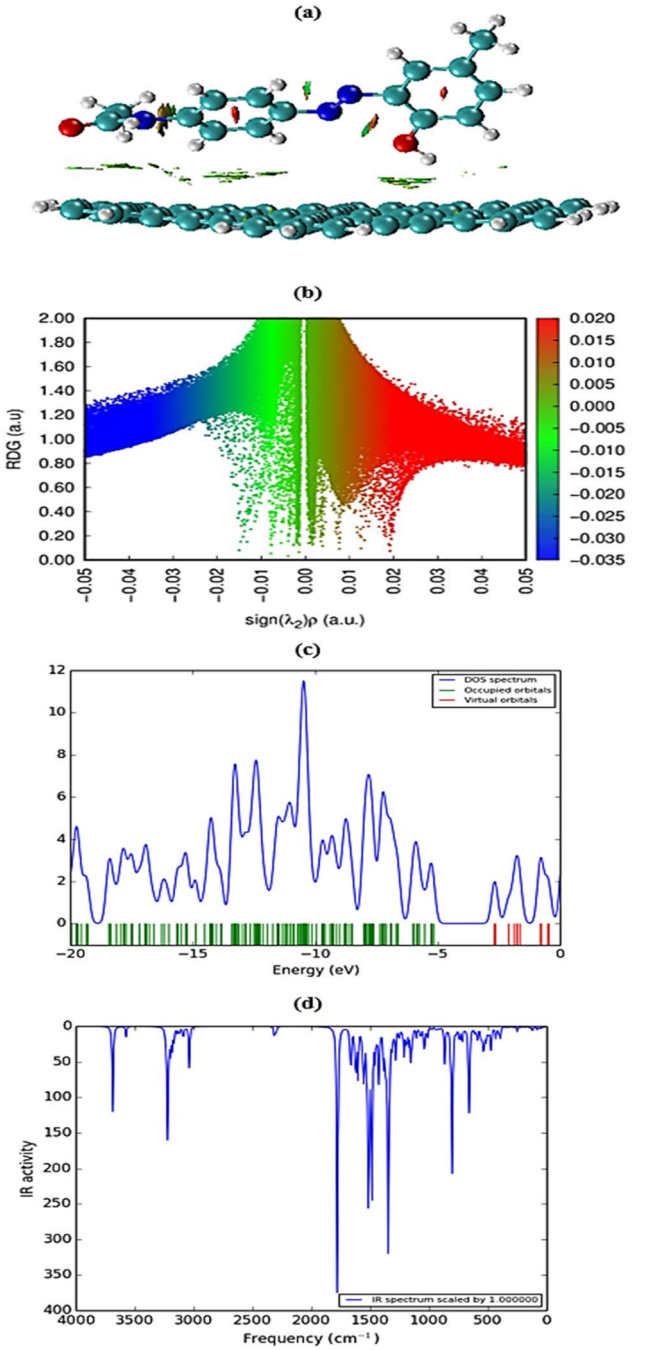

Fig. 2 The Non-Covalent Interaction (NCI) (a), the Reduced Density Gradient (RDG) (b), density of states (DOS) spectra (c), and IR spectra (d) of parallel DY3 dye onto pristine-GDY.

highest among all the Si-GDY configurations, indicating strong electronic interaction. The distribution of electron densities for the HOMO and LUMO of the DY3 dye interacting with Si-GDY in four different binding configurations—(a) parallel, (b) side-parallel, (c) carbonyl-linked, and (d) carbon-linked—are depicted in Fig. 3.

This observation illustrates that the frontier molecular orbitals are primarily concentrated on the DY3 dye molecule with noticeable overlap on the Si-GDY surface, indicating significant electronic interactions between the DY3 dye and the substrate. In the case of the parallel configuration (a), the close proximity and planar alignment between DY3 dye and the Si-GDY indicate favorable conditions for covalent bonding interactions. In the side-parallel configuration (b), the HOMO and LUMO densities spread over a larger area of both the DY3 dye and the Si-GDY, suggesting strong adsorption but with a different interaction nature compared to the direct parallel mode. For the carbonyl-linked (c) and carbon-linked (d) configurations, electron densities are more localized around the bonding regions between the DY3 dye and the Si-GDY surface. This indicates the formation of more specific chemical bonds and possible charge transfer interactions, which can lead to enhanced stability of the adsorption complex.

The DOS spectra for the Si-GDY surface after DY3 dye adsorption are presented in Fig. 4(a–d). Noticeable changes in the electronic states indicate significant electronic interactions between the dye and the doped surface. The electronic parameters are listed in Table 1. The reduction in the HOMO–LUMO gap and the appearance of new states confirm enhanced charge transfer and adsorption stability in the system. The infrared (IR) spectra for the same configurations shown in Fig. 4e–h reveal shifts in vibrational frequencies after adsorption, which indicate molecular interactions at the interface, including bond formation and charge redistribution. These spectral changes are more pronounced in the planar adsorption model, consistent with the stronger adsorption and electronic coupling found in configuration (c). The binding energy for the most stable carbonyl-linked complex is calculated to be −6.00 eV, demonstrating the high stability of this adsorption mode on the Si-GDY surface. Overall, our results indicate that silicon-doping influences the electronic interaction patterns between the DY3 dye and the GDY surface, affecting both the strength and type of binding between the dye and the adsorbent. This influence can directly impact the adsorption efficiency and the electronic properties of the system.

3.3. Reactivity and interaction analysis of DY3 on the Ge-doped GDY surface

Fig. 5(a–d) display the optimized configuration geometries of the DY3 dye molecule adsorbed on the Ge-doped GDY surface. In configuration (a), the molecule lies nearly parallel to the surface with an interaction distance of 2.08 Å. This parallel arrangement enhances π–π stacking between the aromatic rings of the DY3 dye and the surface of GDY. The geometry is stabilized mainly through coordination bonding, as lone pair electrons are donated from the nitrogen atom of the dye to the germanium dopant in the GDY surface. In contrast, configuration (b) adopts a slightly angled orientation with an interaction distance of 1.90 Å. This angle allows better alignment of the dye's coordination with the GDY, enabling coordinate interaction that moderately strengthens the binding. Configuration (c) exhibits nearly perpendicular geometry with an interacting distance of 1.89 Å. In this arrangement, the carbonyl group is oriented directly toward the doped Ge atom. Despite the close proximity, this interaction does not yield the most stable

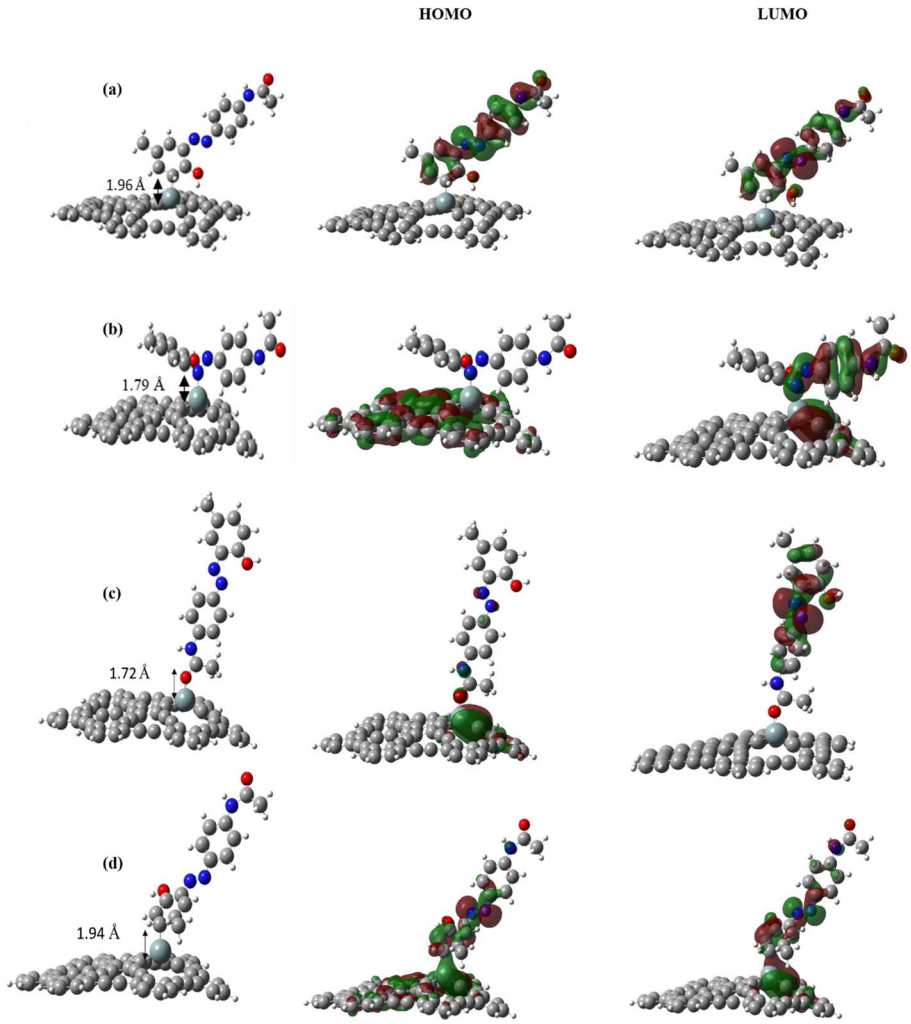

Fig. 3 The optimized models of DY3 dye onto Si-GDY (a–d) and their HOMO and LUMO with various orientations: (a) parallel, (b) side-parallel, (c) carbonyl-linked, and (d) carbon-linked.

configuration. Configuration (d) shows a carbon-linked binding mode, with the molecule oriented side-parallel at an interacting distance of 2.01 Å. This configuration enables significant π-orbital coupling and enhanced electronic interactions, yielding the highest adsorption energy among all configurations. These results confirm that configuration (d) represents the most thermodynamically favorable adsorption geometry on the Ge-GDY surface. The calculated binding energy for the most stable configuration (d), featuring a carbon-linked dye, is −5.68 eV. This value confirms the strongest interaction and highest thermodynamic stability among the examined geometries. To assess the impact of the DY3 dye binding on the electron density distribution in Ge-GDY, we analyzed the HOMO and LUMO of the Ge-GDY/DY3 system (see Fig. 5). Notably, under aqueous conditions, the adsorption behavior of DY3 on Ge-GDY shows a significant stability shift compared to vacuum conditions.

The DOS plots (Fig. 6a–d) show shifts in electronic states and a narrowed HOMO–LUMO gap, confirming charge redistribution and orbital hybridization upon adsorption. Furthermore, the IR spectra (Fig. 6e–h) display altered vibrational modes, including red shifts of C=O stretching frequencies, which corroborate the formation of chemical interactions beyond simple physisorption.

3.4. Exploring non-covalent interactions: insights from reduced density gradient analysis

To elucidate the adsorption mechanism, we performed Non-Covalent Interaction (NCI) analysis and Reduced Density Gradient (RDG) mapping for the DY3 dye adsorbed on pristine-GDY, Si-GDY, and Ge-GDY under vacuum conditions. These visual tools clearly differentiate weak interactions—including hydrogen bonding, van der Waals forces (vdW), and steric repulsions—providing critical insights into the stability and nature of the dye–surface interactions.[105,106] The RDG is derived from the electron density (ρ) and its gradient, as defined by eqn (3):

$$\mathrm{RDG} = \frac{1}{2(3\pi^2)^{1/3}} \frac{|\nabla\rho|}{\rho^{4/3}} \quad (3)$$

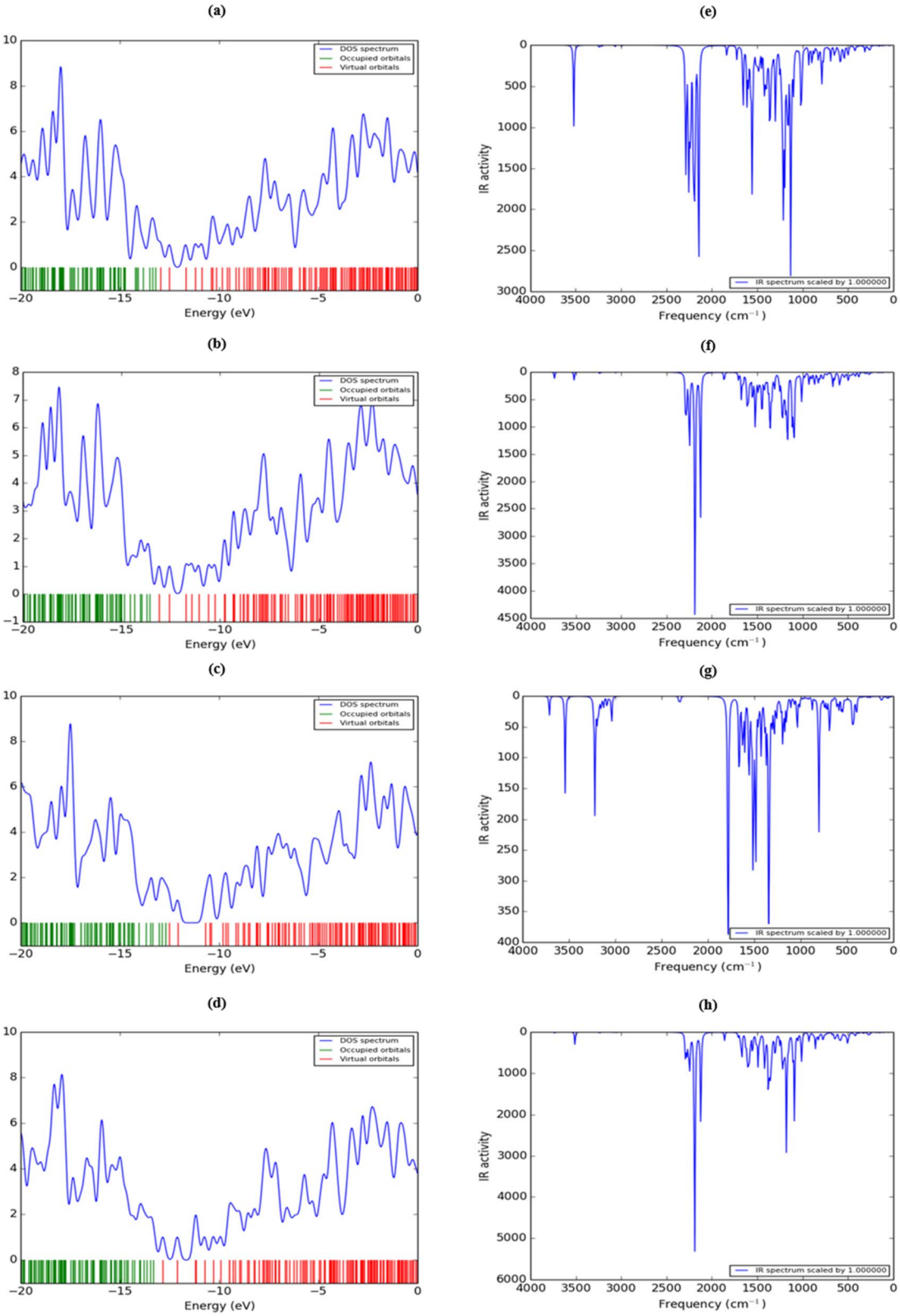

Fig. 4 The density of states (DOS) spectra (a–d), as well as IR spectra (e–h) of DY3 dye onto Si-GDY with different orientations, which are parallel, side-parallel, carbonyl-linked, and carbon-linked, respectively.

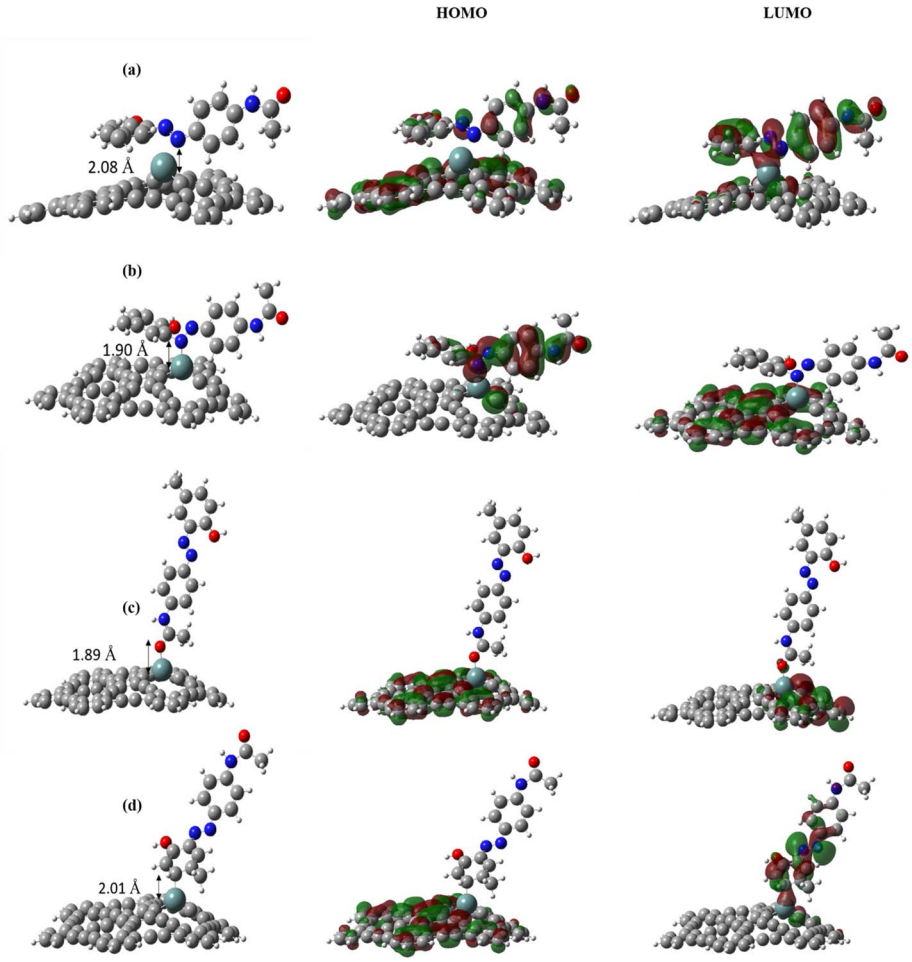

Fig. 5 The optimized models of DY3 dye onto Ge-GDY (a–d) and their HOMO and LUMO with various orientations: (a) parallel, (b) side-parallel, (c) carbonyl-linked, and (d) carbon-linked.

Analysis of RDG *versus* sign(λ_2)ρ plots enables identification of interaction types:

- Negative sign(λ_2)ρ values (green–blue regions) correspond to attractive forces (*e.g.*, hydrogen bonding and π–π interactions).
- Positive values (red regions) indicate steric repulsion.
- When ρ approaches zero, the interactions are characteristic of van der Waals forces.

The RDG plots serve as a powerful tool for analyzing both attractive and repulsive molecular interactions and quantifying their strength.[107] Fig. 7 and 8 present the RDG–NCI analysis for the DY3 dye on Si-GDY and Ge-GDY systems, respectively. All configurations show green RDG iso-surfaces, confirming van der Waals dominance between the dye molecules and the GDY surfaces. Notably, parallel configurations in both systems exhibit more intense blue regions in NCI plots, indicating stronger attractive forces and significant orbital overlap—characteristics consistent with localized chemisorption behavior. These findings confirm that both adsorption geometry and molecular orientation critically determine the interaction mechanism: while parallel alignments favor van der Waals forces, specific directional interactions (*e.g.*, carbonyl linkages) promote charge transfer characteristic of chemisorption. Collectively, NCI–RDG analysis offers profound insights into molecular interactions and adsorption behavior on doped GDY surfaces.

3.5. Global index parameters

We calculated global reactivity descriptors, including electron affinity (EA), ionization potential (IP), electrophilicity index (ω), chemical potential (μ_{ch}), chemical hardness (η), and softness (χ) to assess the electronic reactivity and stability of the system. These global indices provide essential insights into the nature of molecular interactions and reactivity of DY3 dye with GDY. Their respective expressions are given below:[101,108]

Electron affinity (EA) indicates a molecule's ability to accept electrons (LUMO energy):

$$\mathrm{EA} = -E_{\mathrm{L}} \tag{4}$$

The ionization potential (IP) indicates a molecule's ability to donate electrons (HOMO energy):

$$\mathrm{IP} = -E_{\mathrm{H}} \tag{5}$$

The electrophilicity index (ω) reflects a molecule's tendency to accept electrons to form bonds with nucleophilic molecules:

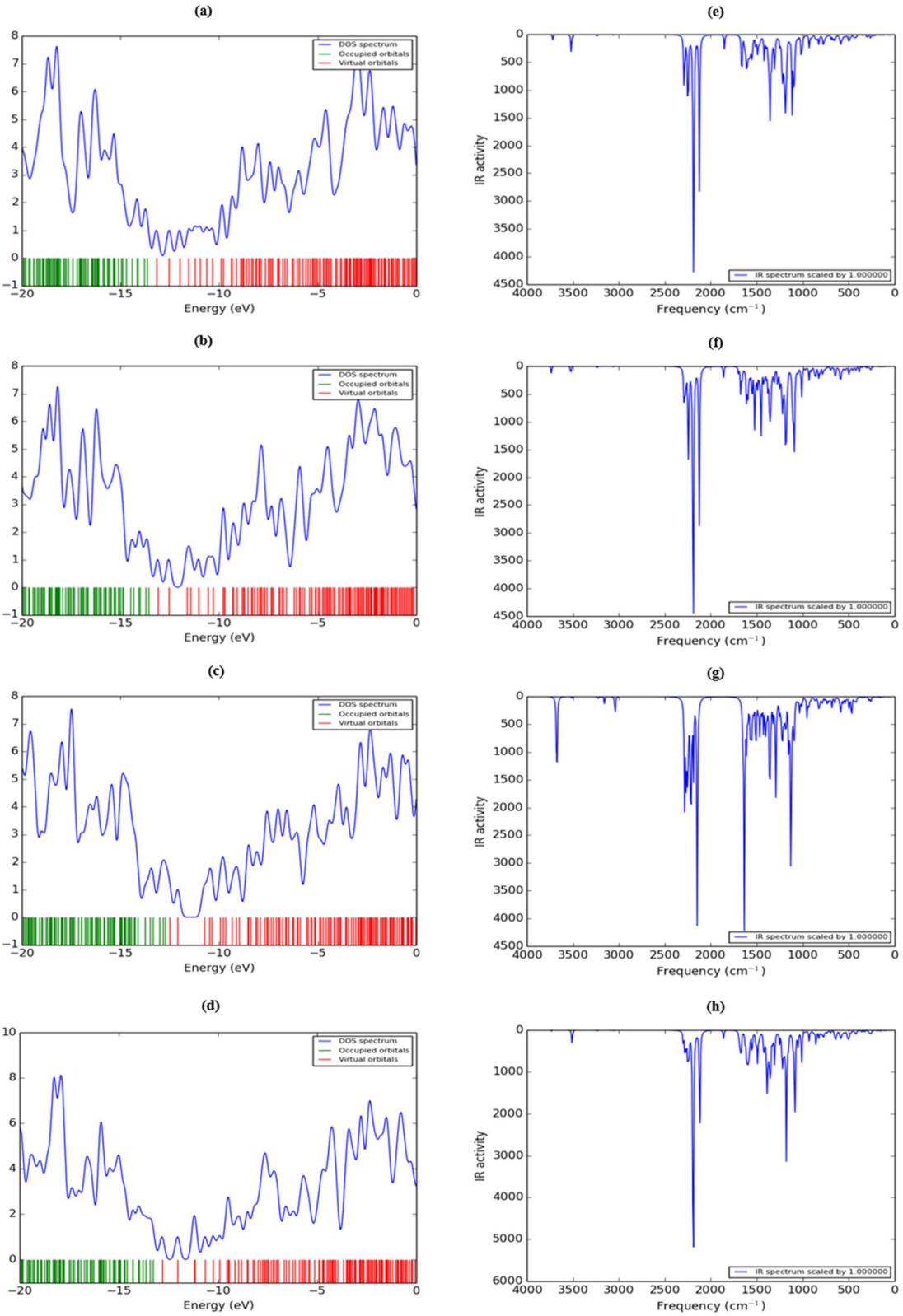

Fig. 6 The density of states (DOS) spectra (a–d), as well as IR spectra (e–h) of DY3 dye onto Ge-GDY with different orientations, which are parallel, side-parallel, carbonyl-linked, and carbon-linked, respectively.

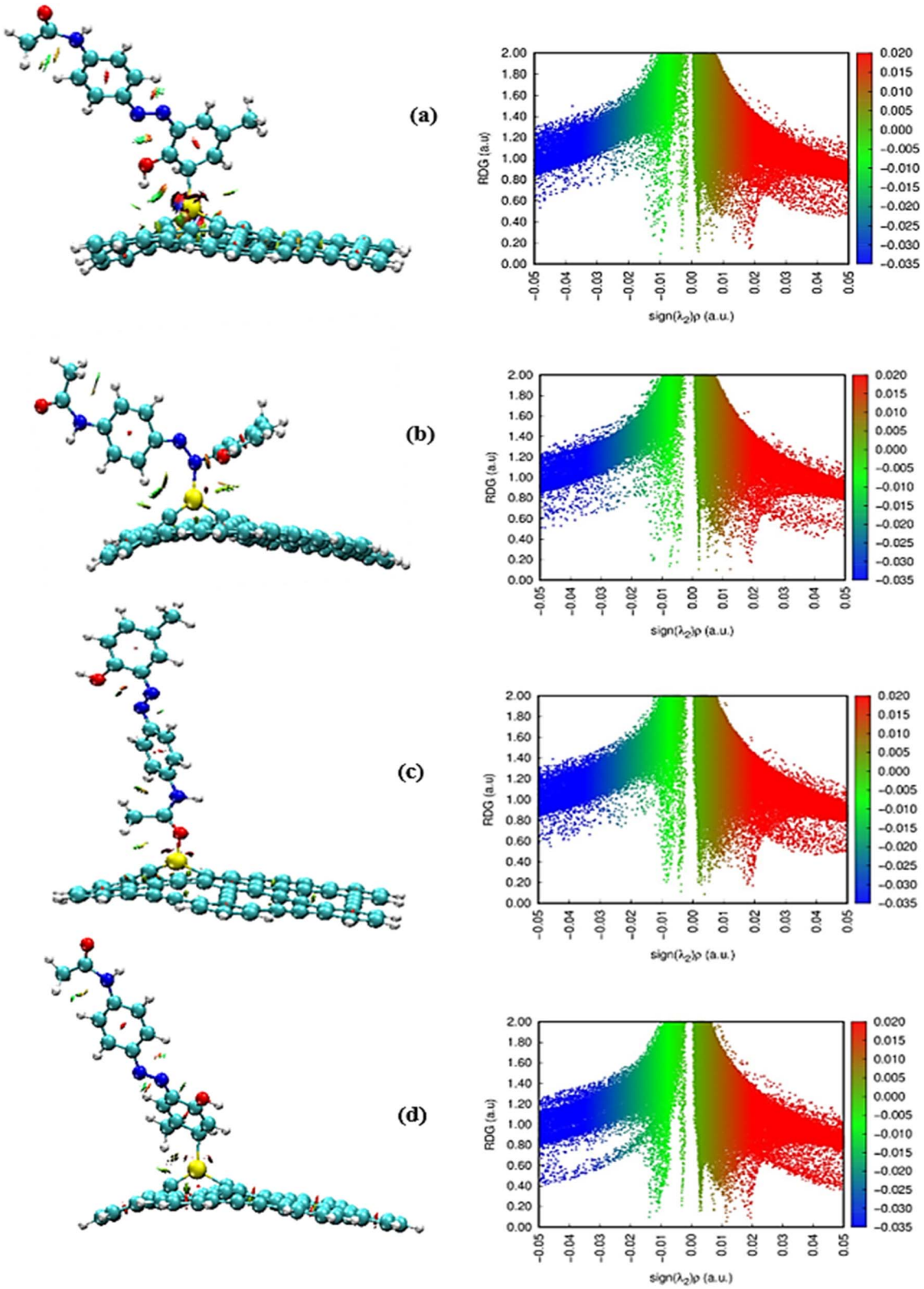

Fig. 7 The Non-Covalent Interaction (NCI) (left) and the Reduced Density Gradient (RDG) (right) in vacuum of the adsorption of DY3 dye on Si-GDY with various configurations: (a) parallel, (b) side-parallel, (c) carbonyl-linked, and (d) carbon-linked.

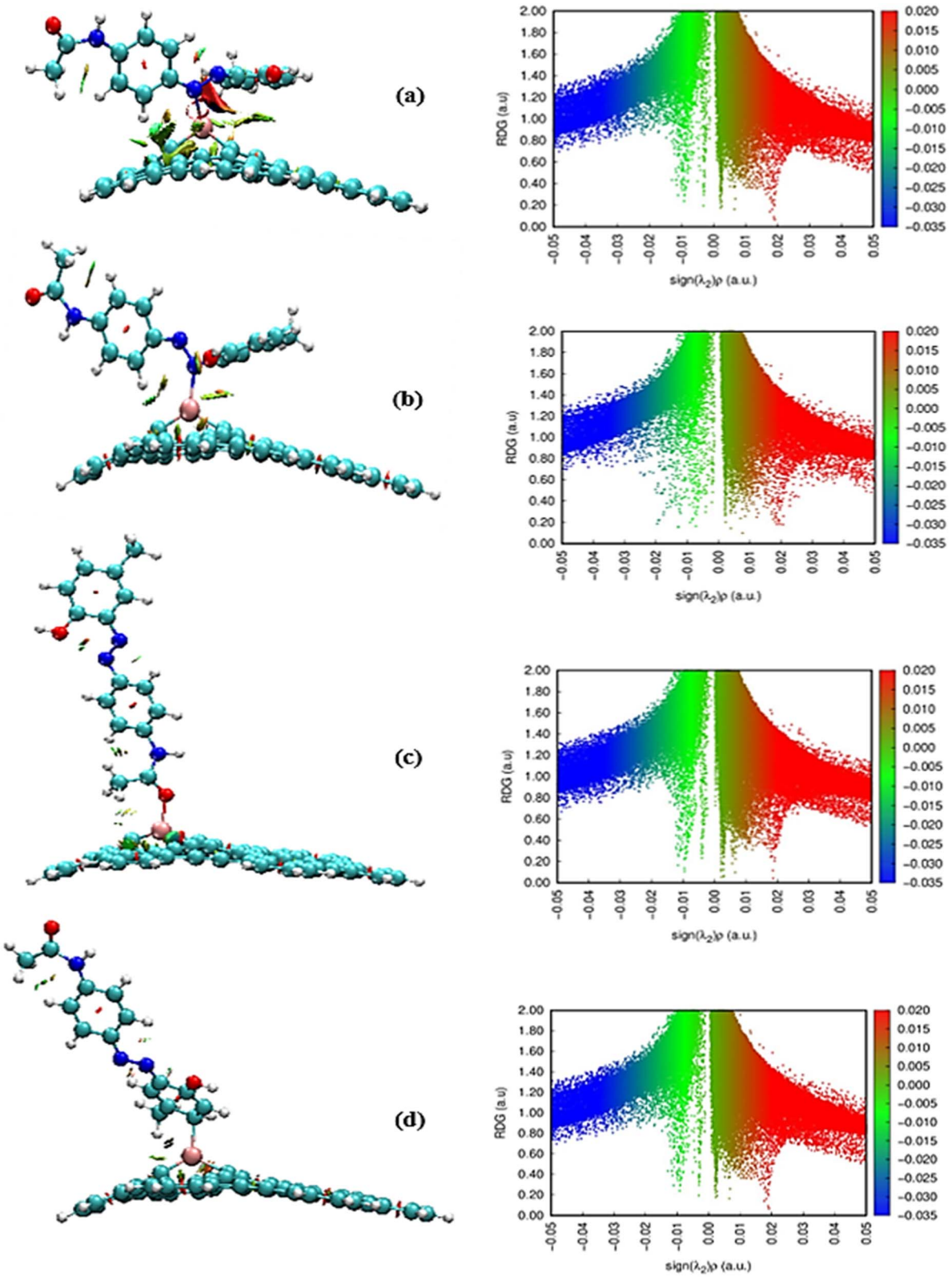

Fig. 8 The Non-Covalent Interaction (NCI) (left) and the Reduced Density Gradient (RDG) (right) in vacuum of the adsorption of DY3 dye on Ge-GDY with various configurations: (a) parallel, (b) side-parallel, (c) carbonyl-linked, and (d) carbon-linked.

$$\omega = \frac{\mu^2}{2\eta} \quad (6)$$

Additionally, the HOMO and LUMO, along with the molecular electrostatic potential (MESP), are sometimes used to enhance the prediction of the adsorption mechanism.[109–114]

$$\text{Chemical potential}(\mu_{ch}): \ \mu_{ch} = \frac{-(\text{IP} + \text{EA})}{2} \quad (7)$$

$$\text{Chemical hardness}(\eta): \ \eta = \frac{(\text{IP} - \text{EA})}{2} \quad (8)$$

$$\text{Softness}(\chi): \ \chi = \frac{1}{\eta} \quad (9)$$

3.6. Thermodynamic parameters: understanding stability and energy changes

The thermodynamic parameters of the optimized complexes were determined through harmonic frequency analysis under standard conditions (298.15 K and 1 atm). Gibbs free energy (ΔG), enthalpy (ΔH) and entropy (ΔS) values for all three orientationally distinct complexes are summarized in Table 2. The relative stability of the inclusion complexes was assessed by comparing the Gibbs free energy of each complex to the combined Gibbs free energies of its adsorbent and adsorbate. Negative ΔG values confirm spontaneous complex formation at 25 °C, whereas positive ΔG values for pristine-GDY complexes indicate non-spontaneous processes. To drive spontaneous complexation and improve efficiency, strategic doping (*e.g.*, with Si or Ge) is proposed.

The negative values of both enthalpy (ΔH) and entropy (ΔS) suggest an enthalpy-driven inclusion process. The observed ΔH likely arises from van der Waals interaction between the host and guest molecules. Meanwhile, the negative ΔS reflects restricted mobility of the encapsulated guest molecule due to the constrained cavity of the host framework.

Table 2 The calculated thermodynamic parameters, enthalpy (ΔH), Gibbs free energy (ΔG), and entropy (ΔS), of the studied complexes DY3/GDY, DY3/Si-GDY, and DY3/Ge-GDY with different orientations in vacuum

System	ΔH (kJ mol^{-1})	ΔG (kJ mol^{-1})	ΔS (kJ mol^{-1})
Parallel	−15.09	29.45	−0.15
Side-parallel	−14.03	21.90	−0.12
Carbon-linked	−9.11	27.46	−0.12
Carbonyl-linked	−4.62	26.24	−0.10
Si-GDY			
Parallel	−444.98	−409.68	−0.12
Side-parallel	−485.24	−448.56	−0.12
Carbon-linked	−547.17	−503.99	−0.14
Carbonyl-linked	−563.75	−518.43	−0.15
Ge-GDY			
Parallel	−415.24	−370.37	−0.15
Side-parallel	−462.64	−426.96	−0.12
Carbon-linked	−527.87	−492.30	−0.12
Carbonyl-linked	−503.71	−459.21	−0.13

$$\Delta G = G_{com} - (G_{host} + G_{guest}) \quad (10)$$

$$\Delta H = H_{com} - (H_{host} + H_{guest}) \quad (11)$$

$$\Delta S = S_{com} - (S_{host} + S_{guest}) \quad (12)$$

3.7. The natural bond orbital analysis for the complexes

Natural Bond Orbital (NBO) charge analysis serves as a vital tool for gaining comprehension of the molecule–molecule interactions between the GDY nanosheet and the DY3 dye molecules in their optimized geometries during the binding process. The NBO analysis was performed to offer detailed insights into the interactions between the localized Lewis-type structures (donors) and the corresponding unoccupied non-Lewis orbitals (acceptors) within the drug–sensor complexes. The interaction parameters, including the second-order perturbation stabilization energy ($E^{(2)}$), the energy difference between donor and acceptor orbitals ($E_{(j)} - E_{(i)}$), and the Fock matrix element ($F_{(i,j)}$), were computed using the DFT/B3LYP/6-31G(d) method. These parameters for each model of complexes are summarized in Table 3. The second-order stabilization energy ($E^{(2)}$), estimated from the Fock matrix, quantifies the delocalization energy associated with donor (i) to acceptor (j) orbital interactions and is calculated using the following expression:

$$E^{(2)} = q_i \frac{F_{(i,j)}{}^2}{E_j - E_i} \quad (13)$$

In the above equation, q_i presents the occupancy of the donor orbital, $E_{(j)}$ and $E_{(i)}$ are the diagonal elements corresponding to the acceptor and donor orbitals, respectively, and $F_{(i,j)}$ denotes the off-diagonal NBO Fock matrix element. The second-order perturbation stabilization energy ($E^{(2)}$) is directly proportional to the intensity of the donor–acceptor interaction. A stronger donor–acceptor interaction leads to a larger $E^{(2)}$ value, thereby increasing the overall stability of the GDY-dye complexes. Consequently, larger $E^{(2)}$ values indicate stronger orbital mixing and charge transfer (chemically significant coordination) while very small $E^{(2)}$ values are consistent with weak, physisorption-like interactions. The stabilization energies $E^{(2)}$ indicate that pristine GDY exhibits only very weak orbital interactions, with the smallest value in the side-parallel geometry (0.16 kcal mol^{-1}), consistent with physisorption. In contrast, Si- and Ge-doped GDY show much stronger donor–acceptor interactions, especially when lone pairs (LP) on O or N atoms of the DY3 dye molecules act as the donor and interact with empty orbitals on Si or Ge atoms on GDY. The strongest stabilization is observed for the Si-GDY carbonyl-linked complex (LP(O) → LP*(Si), 173.99 kcal mol^{-1}), indicating strong covalent coordination, while Ge-GDY parallel and side-parallel geometries also display large values (122.88 and 136.98 kcal mol^{-1}, respectively). Some geometries, such as Ge-GDY carbon-linked (8.63 kcal mol^{-1}), remain relatively weak. Overall, the results reveal a clear trend: pristine GDY favors weak physisorption,

Table 3 The results of the donor and acceptor NBOs, as well as the second-order perturbation stabilization energies ($E^{(2)}$, kcal mol^{-1}), corresponding to the charge transfer between GDY and the DY3 dye molecules in vacuum

System	Donor NBO (i)	Acceptor NBO (j)	$E^{(2)}$ (kcal mol^{-1})	$E_{(j)} - E_{(i)}$ (a.u.)	$F_{(i,j)}$ (a.u.)
Parallel	BD (3) C 34–C 80	BD*(1) O 118–H 119	0.90	0.023	0.007
Side-parallel	BD (2) C 3–C 4	BD*(1) C 99–H 101	0.16	0.71	0.010
Carbon-linked	LP (1) N 104	BD*(1) C 5–H 9	0.96	0.91	0.027
Carbonyl-linked	BD (3) C 68–C 92	BD*(1) N 11–H 12	1.06	0.73	0.026
Si-GDY					
Parallel	LP*(1) Si 84	BD*(1) Si 84–C 110	11.98	0.03	0.032
Side-parallel	LP (2) N 102	LP*(1) Si 119	18.70	0.33	0.072
Carbon-linked	LP*(1) Si 84	BD*(1) Si 84–C 111	74.29	0.03	0.073
Carbonyl-linked	LP (3) O 13	LP*(1) Si 119	173.99	0.72	0.319
Ge-GDY					
Parallel	LP (1) N 102	LP*(2) Ge 119	122.88	0.44	0.213
Side-parallel	LP (1) N 102	LP*(1) Ge 119	136.98	0.44	0.221
Carbon-linked	BD (1) Ge 84–C 111	BD*(1) C 25–Ge 84	8.63	0.66	0.069
Carbonyl-linked	LP (3) O 13	LP*(2) Ge 119	95.21	0.48	0.193

whereas silicon and germanium doping enables much stronger chemisorption when orbital alignment and donor lone pairs are available.

3.7.1 Solvent effect. To evaluate the sensing performance of pristine GDY, Si-GDY, and Ge-GDY in an aqueous environment, we investigated the binding energies (E_{ads}) of DY3 dye complexes in water. The geometries of DY3-GDY, DY3-SiGDY, and DY3-GeGDY complexes were re-optimized using the IEFPCM solvation model, the hybrid B3LYP functional and the 6-31G(d) basis set. Additionally, global reactivity index parameters (Table S1) were computed to further elucidate the electronic properties of the systems. When water effects are considered, the side-parallel configuration for the pristine GDY surface becomes the most stable, with an adsorption energy of −0.10 eV. Compared to vacuum, the aqueous environment slightly weakens the adsorption strength but still preserves sufficient stability, indicating that dye–surface interactions remain strong and persistent under realistic solvent conditions.

For the Si-doped GDY system, considering implicit water significantly alters the adsorption behavior and the carbonyl-linked configuration becomes the most thermodynamically favorable, with a binding energy of −3.87 eV. These findings underline the role of silicon doping in modifying the interaction landscape between the DY3 dye and the GDY surface, thereby influencing both the strength and nature of adsorption. Similarly, in the case of Ge-doped GDY, the side-parallel configuration becomes the most stable, exhibiting an adsorption energy of −3.38 eV. This is in contrast to the vacuum phase, where the carbon-linked mode was more stable. The observed stabilization in water arises from enhanced dipolar alignment and favorable electrostatic interactions between the dye and the doped surface.

Overall, the stability trends observed in vacuum generally align with adsorption energy preferences, such as the dominance of the carbonyl-linked mode in Si-GDY. Upon solvation, particularly in water, noticeable shifts in the thermodynamic preference of the adsorption configurations are observed. This indicates that the solvent influences the relative stability of the complexes by modifying specific interaction mechanisms, such as dipole–dipole interactions and charge-transfer effects. However, the influence of implicit water on the overall adsorption strength remains limited, as it does not drastically weaken the dye–surface interactions but rather induces a reordering of the thermodynamic stability among the possible configurations. The thermodynamic parameter (ΔH) calculated for the carbonyl-linked configurations of Si-GDY and Ge-GDY in the solvent phase exhibit unusually high positive values (Table S1). Such positive enthalpies clearly indicate that this binding mode is thermodynamically unfavorable in implicit water. This result highlights the strong environmental sensitivity of the doped systems, where solvation effects destabilize the carbonyl-linked interactions compared to their gas-phase counterparts. The findings underscore the critical role of the solvent in modulating adsorption behavior and provide valuable insight into the selective stability of different binding modes under realistic conditions.

The comparative analysis between vacuum and aqueous conditions (Fig. S3–S5 for pristine GDY, Si-GDY, and Ge-GDY, respectively) further confirms that water modulates the stability trends without significantly diminishing the adsorption strength. Thus, the adsorption configurations remain stable across different environments, with solvation exerting a qualitative influence on the relative energetic ordering rather than a substantial reduction in interaction strength.

3.8. Comparison of adsorption energy (E_{ads}) and adsorption distance (d) of disperse yellow 3 dye adsorbed on pristine GDY, Si-GDY and Ge-GDY with previously reported materials

A comprehensive comparison of the adsorption energies (E_{bind}) and adsorption distances (d) for various dyes, drugs, and gas molecules on a range of nanomaterials, with particular focus on pristine and doped-GDY systems is shown in Table 4. For dyes

Table 4 Comparison of adsorption energy (E_{ads}) and adsorption distance (d) for dyes or drugs adsorbed on pristine or doped-GDY with those reported for other nanomaterials

System	E_{bind} (eV)	d (Å)	References
DY3 dye			
GDY	−0.21	4.49	This work
Si-GDY	−6.00	1.72	This work
Ge-GDY	−5.68	1.89	This work
Reduced graphene oxide (rGO)			
Methylene blue (MB) dye	−1.94	—	115
Indigo carmine (IC) dye	−1.62	—	115
Graphene oxide (GO)			
Methylene blue	−2.25	—	116
Methyl orange	−1.45	—	116
Mn–N-GDY			
Methane (CH_4)	−0.16	1.53	117
Temozolomide (TMZ) drug			
Boron-doped GDY (BGDY)	−0.95	1.98	41
GDY	−0.50	2.06	41
5-Fluorouracil (FU) drug			
GDY	−0.42	2.10	118
BNGDY	−0.60	1.68	118
Hydroxyurea (HU) drug			
GDY	−0.60	2.30	118
BNGDY	−1.29	0.16	118
Thioguanine (TG) drug			
Graphyne (GY)	−0.19	1.70	97
BN-analog of GY (BNY)	−5.4	1.67	97
A-series CWAs on GDY nanoflakes			
A-230	−0.59	2.59	119
A-232	−0.71	2.66	119
A-234	−0.75	2.97	119
Thiotepa (TPA) drug			
GDY	−0.42	—	96
Si-GDY	−0.81	—	96
Letrozole (LET) drug			
GDY	−0.33	—	120
Si-GDY	−0.83	—	120
Graphene quantum dots (GQDs)			
CO_2	−0.54	3.81	121
H_2S	−0.53	5.31	121
Cr-doped GQDs			
CO_2	−3.81	2.03	121
H_2S	−3.56	2.36	121
Ni- doped GQDs			
CO_2	−0.08	3.22	121
H_2S	−0.10	2.84	121

such as DY3, pristine GDY exhibits weak interaction with a low adsorption energy of −0.21 eV. In contrast, Si-GDY and Ge-GDY demonstrate significantly enhanced adsorption energies of −6.00 and −5.68 eV, respectively, coupled with shorter adsorption distances, indicating stronger binding due to doping. Graphene oxide (GO) and reduced graphene oxide (rGO) display moderate adsorption energies with dyes like methylene blue (MB) and indigo carmine (IC), at −1.94 and −1.62 eV, respectively, reflecting weaker interactions compared to doped GDY. Mn–N-GDY shows weak physical adsorption of methane with an energy of −0.16 eV and a short adsorption distance of 1.53 Å. Regarding drug adsorption, significant differences are noted across materials. Temozolomide (TMZ) adsorbs moderately on boron-doped GDY (BGDY) with an adsorption energy of −0.95 eV and a distance of 1.98 Å, compared to much lower adsorption on pristine GDY (−0.50 eV), highlighting the effect of doping. Similarly, 5-fluorouracil (FU) shows improved adsorption from −0.42 eV on GDY to −0.60 eV on boron–nitrogen-doped GDY (BNGDY), with a decreased adsorption distance from 2.10 to 1.68 Å, indicating enhanced interaction. Hydroxyurea (HU) exhibits a strong enhancement with doping: the adsorption energy increases from −0.60 eV on GDY to −1.29 eV on BNGDY, while the adsorption distance significantly decreases from 2.30 to 0.16 Å, reflecting stronger chemical interaction. Extending the comparison, thioguanine (TG) shows an increase in adsorption energy from −0.19 eV on graphyne (GY) to −5.4 eV on boron–nitrogen-doped GDY (BNY).

The adsorption energies (E_{ad}) for the A-series CWAs on GDY nanoflake are all negative, indicating thermodynamically favorable interactions. Among them, A-234 exhibits the strongest interaction with an E_{ad} of −0.75 eV, followed by A-232 and A-230. This trend suggests an increasing adsorption strength across the series. For the drug thiotepa (TPA), its adsorption on pristine GDY shows an E_{ad} of −0.42 eV, whereas doping Si-GDY significantly enhances the adsorption strength to −0.81 eV. Letrozole (LET) demonstrates a significant increase in binding strength from −0.33 eV on GDY to −0.83 eV on Si-GDY, further confirming the role of doping in improving surface reactivity. For gas molecules, chromium-doped graphene quantum dots (Cr-GQDs) exhibit very high adsorption energies, such as −3.81 eV for CO_2, far exceeding those on undoped GQDs (−0.54 eV). Similarly, nickel-doped graphene quantum dots (Ni-GQDs) show strong adsorption with energies up to −0.10 eV, emphasizing the effectiveness of transition metal doping in enhancing adsorption capacity. Overall, Si-GDY, Cr-GQDs, and Ni-GQDs demonstrate the highest adsorption energies among the studied systems, indicating superior thermodynamic stability and strong binding affinity. These findings highlight the critical role of doping and surface modification as effective strategies to enhance adsorption performance, positioning these materials as excellent candidates for applications in sensing, drug delivery, and environmental remediation.

4. Conclusion

This study investigated the adsorption behavior of DY3 dye on pristine-GDY and its silicon and germanium doped variants using DFT calculations. Various adsorption models, including parallel, side-parallel, carbon-linked, and carbonyl-linked

configurations, were optimized to identify the most stable structures. The results demonstrated that doping significantly enhanced electronic interactions between the DY3 dye and the surface of GDY, increasing adsorption energy and reducing the HOMO–LUMO gap, which indicates improved electronic performance. For DY3/pristine-GDY, the parallel configuration was found to be the most stable, with an adsorption energy of −0.21 eV. The DY3/Si-GDY with carbonyl linked configuration showed the highest adsorption energy of −6.00 eV, suggesting a strong chemisorption interaction. This configuration exhibited stronger electronic interactions and broader orbital delocalization. DY3/Ge-GDY showed that the carbon-linked configuration is more stable and favorable with a binding energy of −5.68 eV. Comparison across all systems revealed that doping not only strengthens adsorption but also modifies the electronic structure of GDY, promoting better charge transfer and molecular reactivity. HOMO–LUMO distributions showed significant orbital overlap between the DY3 dye and the surface, supported by clear changes in DOS spectra and IR vibrational shifts. RDG–NCI analysis further revealed strong attractive regions and van der Waals interactions. Based on the computed results, silicon doping was found to be more effective than germanium doping, as Si-GDY exhibited stronger electronic interactions, broader orbital distributions, and higher adsorption energy, particularly in the carbonyl-linked configuration, indicating better dye stabilization and enhanced adsorption behavior. Moreover, simulations conducted in an aqueous phase using the IEFPCM model showed minimal changes in geometry and adsorption energy, confirming the environmental stability and reliability of the studied systems under realistic conditions. The study also examined thermodynamic parameters, including changes in Gibbs free energy, enthalpy, and entropy, which supported the spontaneous and stable nature of the adsorption process in most stable configurations. The results indicated that doping significantly enhanced the sensing performance, suggesting potential applications in environmental monitoring. Overall, this study confirms that doping GDY with Si or Ge effectively enhances its physical and chemical properties, making it a promising candidate for environmental remediation applications, especially for the removal of stable and toxic industrial dyes from wastewater. The findings provide a theoretical foundation for the design of advanced adsorbent and sensor materials that are efficient, selective, and environment friendly.

Author contributions

Mohamed M. Aboelnga: supervision, validation, conceptualization, project administration, computational analysis, investigation, visualization, data analysis, software, resources, writing –review & editing. Mariam M. Seliem: computational analysis, investigation, data curation, visualization, formal analysis, methodology, writing – original draft. Elsayed El-Bayoumy: supervision, validation, conceptualization, writing – review & editing. Mohsen El-Tahawy: supervision, validation, conceptualization, computational analysis, investigation, visualization, data analysis, software, resources, writing – review & editing.

Conflicts of interest

The authors declare that they have no known competing financial interests or personal relationships that could have appeared to influence the work reported in this paper.

Data availability

Additional computational input and output files, including geometry optimizations and electronic structure data, are available from the corresponding author upon reasonable request. Most of the optimization files have been collected in this Google Drive link (**https://drive.google.com/file/d/1d2pogVTnGz5h0d_HvOd9oCRjFBNNBeqO/view?usp=drive_link**).

All data supporting the findings of this study are available within the article and its SI. Supplementary information is available. See DOI: **https://doi.org/10.1039/d5na00720h**.

Acknowledgements

This research did not receive any specific grant from funding agencies in the public, commercial, or not-for-profit sectors.

References

1 K. N. Aboua, Y. A. Yobouet, K. B. Yao, D. L. Goné and A. Trokourey, Investigation of dye adsorption onto activated carbon from the shells of Macoré fruit, *J. Environ. Manage.*, 2015, **156**, 10–14.
2 C. Djilani, R. Zaghdoudi, F. Djazi, B. Bouchekima, A. Lallam, A. Modarressi, *et al.*, Adsorption of dyes on activated carbon prepared from apricot stones and commercial activated carbon, *J. Taiwan Inst. Chem. Eng.*, 2015, **53**, 112–121.
3 C. Jiang, X. Wang, D. Qin, W. Da, B. Hou, C. Hao, *et al.*, Construction of magnetic lignin-based adsorbent and its adsorption properties for dyes, *J. Hazard. Mater.*, 2019, **369**, 50–61.
4 Z. Jiang and D. Hu, Molecular mechanism of anionic dyes adsorption on cationized rice husk cellulose from agricultural wastes, *J. Mol. Liq.*, 2019, **276**, 105–114.
5 A. M. Aljeboree, A. N. Alshirifi and A. F. Alkaim, Kinetics and equilibrium study for the adsorption of textile dyes on coconut shell activated carbon, *Arabian J. Chem.*, 2017, **10**, S3381–S3393.
6 H. S. Freeman and G. N. Mock, Dye application, manufacture of dye intermediates and dyes, *Kent and Riegel's Handbook of Industrial Chemistry and Biotechnology*, 2007, pp. 499–590.
7 M. Lewin, *Handbook of Fiber Chemistry*, Crc press, 2006.
8 T. P. Cameron, T. J. Hughes, P. E. Kirby, V. A. Fung and V. C. Dunkel, Mutagenic activity of 27 dyes and related chemicals in the Salmonella/microsome and mouse

lymphoma TK+/− assays, *Mutat. Res., Genet. Toxicol.*, 1987, **189**(3), 223–261.
9 A. Bafana, S. S. Devi and T. Chakrabarti, Azo dyes: past, present and the future, *Environ. Rev.*, 2011, **19**(NA), 350–371.
10 I. Hussain, Y. Li, J. Qi, J. Li and L. Wang, Nitrogen-enriched carbon sheet for Methyl blue dye adsorption, *J. Environ. Manage.*, 2018, **215**, 123–131.
11 S. Wong, N. A. N. Yac'cob, N. Ngadi, O. Hassan and I. M. Inuwa, From pollutant to solution of wastewater pollution: Synthesis of activated carbon from textile sludge for dye adsorption, *Chin. J. Chem. Eng.*, 2018, **26**(4), 870–878.
12 J. Fu, J. Zhu, Z. Wang, Y. Wang, S. Wang, R. Yan, *et al.*, Highly-efficient and selective adsorption of anionic dyes onto hollow polymer microcapsules having a high surface-density of amino groups: Isotherms, kinetics, thermodynamics and mechanism, *J. Colloid Interface Sci.*, 2019, **542**, 123–135.
13 H. Marsh and F. R. Reinoso, *Activated Carbon*, Elsevier, 2006.
14 C. S. Cundy and P. A. Cox, The hydrothermal synthesis of zeolites: history and development from the earliest days to the present time, *Chem. Rev.*, 2003, **103**(3), 663–702.
15 J. Gregory and S. Barany, Adsorption and flocculation by polymers and polymer mixtures, *Adv. Colloid Interface Sci.*, 2011, **169**(1), 1–12.
16 J. R. Li, J. Sculley and H. C. Zhou, Metal–organic frameworks for separations, *Chem. Rev.*, 2012, **112**(2), 869–932.
17 F. Yavari and N. Koratkar, Graphene-based chemical sensors, *J. Phys. Chem. Lett.*, 2012, **3**(13), 1746–1753.
18 G. Li, Y. Li, H. Liu, Y. Guo, Y. Li and D. Zhu, Architecture of graphdiyne nanoscale films, *Chem. Commun.*, 2010, **46**(19), 3256–3258.
19 V. Nagarajan, U. Srimathi and R. Chandiramouli, First-principles insights on detection of dimethyl amine and trimethyl amine vapors using graphdiyne nanosheets, *Comput. Theor. Chem.*, 2018, **1123**, 119–127.
20 V. Nagarajan and R. Chandiramouli, Alcohol molecules adsorption on graphane nanosheets–a first-principles investigation, *Appl. Surf. Sci.*, 2018, **441**, 734–743.
21 A. S. Rad, Adsorption of mercaptopyridine on the surface of Al-and B-doped graphenes: Theoretical study, *J. Alloys Compd.*, 2016, **682**, 345–351.
22 A. Shokuhi Rad, A. S. Alijantabar, N. Motaghedi, S. Maleki and M. Peyravi, Theoretical study of chemisorption of cyanuric fluoride and S-triazine on the surface of Al-doped graphene, *Mol. Simul.*, 2016, **42**(18), 1519–1527.
23 A. S. Rad, S. M. Aghaei, E. Aali, M. Peyravi and M. Jahanshahi, Application of chromium-doped fullerene as a carrier for thymine and uracil nucleotides: Comprehensive density functional theory calculations, *Appl. Organomet. Chem.*, 2018, **32**(2), e4070.
24 M. S. Hoseininezhad-Namin, P. Pargolghasemi, S. Alimohammadi, A. S. Rad and L. Taqavi, Quantum Chemical Study on the adsorption of metformin drug on the surface of pristine, Si-and Al-doped (5, 5) SWCNTs, *Phys. E*, 2017, **90**, 204–213.
25 S. Gholami, A. S. Rad, A. Heydarinasab and M. Ardjmand, Adsorption of adenine on the surface of nickel-decorated graphene; A DFT study, *J. Alloys Compd.*, 2016, **686**, 662–668.
26 P. Wang, Z. Li, Q. Xie, W. Duan, X. Zhang and H. Han, A passive anti-icing strategy based on a superhydrophobic mesh with extremely low ice adhesion strength, *J. Bionic Eng.*, 2021, **18**, 55–64.
27 X. Gao, H. Liu, D. Wang and J. Zhang, Graphdiyne: synthesis, properties, and applications, *Chem. Soc. Rev.*, 2019, **48**(3), 908–936.
28 G. Li, Y. Li, H. Liu, Y. Guo, Y. Li and D. Zhu, Architecture of graphdiyne nanoscale films, *Chem. Commun.*, 2010, **46**(19), 3256–3258.
29 D. V. Chachkov and O. V. Mikhailov, Novel modifications of elemental nitrogen and their molecular structures–a quantum-chemical calculation, *Structure*, 2020, **5**(109.8), N1N2N3N4.
30 H. Kurban, S. Alaei and M. Kurban, Effect of Mg content on electronic structure, optical and structural properties of amorphous ZnO nanoparticles: A DFTB study, *J. Non-Cryst. Solids*, 2021, **560**, 120726.
31 M. Çadırcı, E. Elibol, T. Demirci and M. Kurban, Investigating the effect of Zn doping and temperature on the photoluminescence behaviour of CuLaSe2 quantum dots, *Luminescence*, 2024, **39**(4), e4722.
32 İ. Muz, F. Göktaş and M. Kurban, Size dependence in the electronic and optical properties of a BN analogue of two-dimensional graphdiyne: A theoretical study, *Chem. Phys.*, 2020, **539**, 110929.
33 İ. Muz and M. Kurban, The electronic structure, transport and structural properties of nitrogen-decorated graphdiyne nanomaterials, *J. Alloys Compd.*, 2020, **842**, 155983.
34 İ. Muz and M. Kurban, Electronic structures and bonding of graphdiyne and its BN analogs: Transition from quasi-planar to planar sheets, *J. Alloys Compd.*, 2020, **846**, 155987.
35 S. Ali and B. Lone, Adsorption of cytosine on Si and Ge doped graphene: A DFT study, in *Materials Today: Proceedings*, Elsevier Ltd, 2023. pp. 774–781.
36 C. Polat, M. Kurban and H. Kurban, Multimodal neural network-based predictive modeling of nanoparticle properties from pure compounds, *Mach. Learn.: Sci. Technol.*, 2024, **5**, 045062.
37 G. Yang, Z. Li, S. Wang and J. Lin, Achieving high quantum capacitance graphdiyne through doping and adsorption, *Phys. Chem. Chem. Phys.*, 2023, **25**(3), 2012–2018.
38 A. Mohajeri and A. Shahsavar, Tailoring the optoelectronic properties of graphyne and graphdiyne: nitrogen/sulfur dual doping versus oxygen containing functional groups, *J. Mater. Sci.*, 2017, **52**, 5366–5379.
39 Y. Feng, M. Sun, Y. Ji and T. Fan, Is Fe the Most Active Site for Fe/N-Doped Graphdiyne?, *ACS Omega*, 2024, **9**(15), 17389–17397.

40 R. Bagheri, M. Babazadeh, E. Vessally, M. Es'haghi and A. Bekhradnia, Si-doped phagraphene as a drug carrier for adrucil anti-cancer drug: DFT studies, *Inorg. Chem. Commun.*, 2018, **90**, 8–14.
41 P. Xu, N. Na and A. Mohamadi, Investigation the application of pristine graphdiyne (GDY) and boron-doped graphdiyne (BGDY) as an electronic sensor for detection of anticancer drug, *Comput. Theor. Chem.*, 2020, **15**, 1190.
42 G. Gecim, M. Ozekmekci and M. F. Fellah, Ga and Ge-doped graphene structures: A DFT study of sensor applications for methanol, *Comput. Theor. Chem.*, 2020, **1180**, 112828.
43 J. He, S. Y. Ma, P. Zhou, C. X. Zhang, C. He and L. Z. Sun, Magnetic properties of single transition-metal atom absorbed graphdiyne and graphyne sheet from DFT+ U calculations, *J. Phys. Chem. C*, 2012, **116**(50), 26313–26321.
44 R. Liu, H. Liu, Y. Li, Y. Yi, X. Shang, S. Zhang, *et al.*, Nitrogen-doped graphdiyne as a metal-free catalyst for high-performance oxygen reduction reactions, *Nanoscale*, 2014, **6**(19), 11336–11343.
45 Y. Zou, F. Li, Z. H. Zhu, M. W. Zhao, X. G. Xu and X. Y. Su, An ab initio study on gas sensing properties of graphene and Si-doped graphene, *Eur. Phys. J. B*, 2011, **81**, 475–479.
46 P. A. Denis, Band gap opening of monolayer and bilayer graphene doped with aluminium, silicon, phosphorus, and sulfur, *Chem. Phys. Lett.*, 2010, **492**(4–6), 251–257.
47 M. D. Esrafili, N. Saeidi and P. Nematollahi, Si-doped graphene: A promising metal-free catalyst for oxidation of SO2, *Chem. Phys. Lett.*, 2016, **649**, 37–43.
48 P. Guo, H. Zhang, S. Dong and L. An, Density functional theory study of B-and Si-doped carbons and their adsorption interactions with sulfur compounds, *Carbon Energy*, 2024, **6**(2), e489.
49 H. Soleymanabadi and S. Alshimaysawee, Evaluation of ibuprofen drug assay using silicon doped graphdiyne: insights from density functional theory, *Mol. Phys.*, 2024, **122**(6), e2261568.
50 G. A. Okon, D. G. Malu, H. Y. Abdullah, C. R. Nwokoye, N. I. Gber and C. P. Egbo, Chalcogenides encapsulated Pt-doped carbon quantum dot (Pt@CQD) as a carrier for the controlled release of lapachone: outlook from theoretical calculations, *Diamond Relat. Mater.*, 2024, **149**, 111628.
51 K. W. Qadir, M. D. Mohammadi and H. Y. Abdullah, Modelling gas adsorption onto Al12(Zn)N12 surfaces: A theoretical study of CH4, CO, CO2, H2O, N2, NH3, NO, NO2, O2, and SO2 interactions, *Comput. Theor. Chem.*, 2025, **1244**, 115063.
52 G. Yu, Y. Xie, Q. Ge, Q. Dai, J. Xu and H. Cao, Mechanism of ozone adsorption and activation on B-, N-, P-, and Si-doped graphene: A DFT study, *Chem. Eng. J.*, 2022, **430**, 133114.
53 F. Behmagham, E. Vessally, B. Massoumi, A. Hosseinian and L. Edjlali, A computational study on the SO2 adsorption by the pristine, Al, and Si doped BN nanosheets, *Superlattices Microstruct.*, 2016, **100**, 350–357.
54 F. Zhao, Y. Feng and W. Feng, Germanium-based monoelemental and binary two-dimensional materials: Theoretical and experimental investigations and promising applications, *InfoMat*, 2022, **4**(11), e12365.
55 Y. Liao, R. Peng, S. Peng, W. Zeng and Q. Zhou, The adsorption of h2 and c2h2 on ge-doped and cr-doped graphene structures: A DFT study, *Nanomaterials*, 2021, **11**(1), 1–14.
56 B. O. Ekpong, H. Y. Abdullah, E. Emmanuel, I. Benjamin and D. C. Agurokpon, Transition metals tailoring of phosphorus-doped gallium nitride nanotubes as sensors for N-butenyl homoserine lactone (BHL): A computational study, *Comput. Theor. Chem.*, 2024, **1241**, 114914.
57 M. Doust Mohammadi, H. Y. Abdullah, H. Louis, E. E. Etim and H. O. Edet, Evaluating the detection potential of C59X fullerenes (X = C, Si, Ge, B, Al, Ga, N, P, and As) for H2SiCl2 molecule, *J. Mol. Liq.*, 2023, **387**, 122621.
58 M. D. Mohammadi, H. Y. Abdullah, H. Louis, E. E. Etim, H. O. Edet and O. C. Godfrey, Hexachlorobenzene (HCB) adsorption onto the surfaces of C60, C59Si, and C59Ge: Insight from DFT, QTAIM, and NCI, *Chem. Phys. Impact*, 2023, **6**, 100234.
59 H. Y. Abdullah, Theoretical study of the binding energy of some gases on Al-doped carbon nanotube, *Results Phys.*, 2016, **6**, 1146–1151.
60 S. Haghgoo and A. Nekoei, Metal oxide adsorption on fullerene C60and its potential for adsorption of pollutant gases; density functional theory studies, *RSC Adv.*, 2021, **11**(28), 17377–17390.
61 W. M. Taha, M. Morsy, N. A. Nada and M. A. Ibrahim, Modeling the electronic properties for CNT interacted with ZnO, CuO, and Co3O4, *Opt. Quantum Electron.*, 2022, **54**, 597.
62 M. Rezazade, S. Ketabi and M. Qomi, Effect of functionalization on the adsorption performance of carbon nanotube as a drug delivery system for imatinib: molecular simulation study, *BMC Chem.*, 2024, **18**, 85.
63 C. R. Girish, Determination of thermodynamic parameters in adsorption studies: a review, *Chemical Papers*, Springer Science and Business Media Deutschland GmbH, 2025.
64 H. Jedli, C. Briki, A. Chrouda, J. Brahmi, A. Abassi, A. Jbara, *et al.*, Experimental and theoretical study of CO2 adsorption by activated clay using statistical physics modeling, *RSC Adv.*, 2019, **9**(66), 38454–38463.
65 A. D. Becke, Density-functional exchange-energy approximation with correct asymptotic behavior, *Phys. Rev. A*, 1988, **38**(6), 3098.
66 Y. S. Al-Hamdani, M. Rossi, D. Alfe, T. Tsatsoulis, B. Ramberger, J. G. Brandenburg, *et al.*, Properties of the water to boron nitride interaction: From zero to two dimensions with benchmark accuracy, *J. Chem. Phys.*, 2017, **147**(4), 044710.
67 W. L. Yu, H. W. Zuo, C. H. Lu, Y. Li, Y. F. Zhang and W. K. Chen, Nitrous oxide decomposition catalyzed by Au19Pd and Au19Pt clusters, *Acta Phys.-Chim. Sin.*, 2015, **31**(3), 425–434.
68 C. Lee, W. Yang and R. G. Parr, Development of the Colle-Salvetti correlation-energy formula into a functional of the

electron density, *Phys. Rev. B: Condens. Matter Mater. Phys.*, 1988, **37**(2), 785.

69 X. Min, W. Li, Z. Wei, R. Spinney, D. D. Dionysiou, Y. Seo, *et al.*, Sorption and biodegradation of pharmaceuticals in aerobic activated sludge system: a combined experimental and theoretical mechanistic study, *Chem. Eng. J.*, 2018, **342**, 211–219.

70 M. M. Aboelnga, J. J. Hayward and J. W. Gauld, A water-mediated and substrate-assisted aminoacylation mechanism in the discriminating aminoacyl-tRNA synthetase GlnRS and non-discriminating GluRS, *Phys. Chem. Chem. Phys.*, 2017, **19**, 25598–25609.

71 M. M. Aboelnga, J. J. Hayward and J. W. Gauld, Unraveling the Critical Role Played by Ado762′OH in the Post-Transfer Editing by Archaeal Threonyl-tRNA Synthetase, *J. Phys. Chem. B*, 2018, **122**, 1092–1101.

72 E. Elbayoumy, M. O. Elassi, G. M. Khairy, E. A. Moawed and M. M. Aboelnga, Development of efficient fluorescent sensor for the detection of hazard aromatic nitro compounds via N-(1-naphthyl)ethylenediamine: experimental and DFT studies, *J. Mol. Liq.*, 2023, **391**, 123270.

73 I. A. Aguayo-Villarreal, D. Cortes-Arriagada, C. K. Rojas-Mayorga, K. Pineda-Urbina, R. Muñiz-Valencia and J. Gonzalez, Importance of the interaction adsorbent–adsorbate in the dyes adsorption process and DFT modeling, *J. Mol. Struct.*, 2020, **1203**, 127398.

74 A. R. Gupta, A. Yadav and S. Sharma, Scavenging fluoride from the aqueous system with porous organometallic three-dimensional architecture: An emerging adsorbent, *Environ. Sci. Pollut. Res.*, 2021, **28**, 19166–19178.

75 F. Xiao, H. Li, P. Xie, J. Liu, W. Du, L. Li, *et al.*, Colloidal templating of highly ordered porous amidoxime-functionalized hydrogel for intelligent treatment of uranium contaminated water, *Chem. Eng. J.*, 2022, **431**, 134141.

76 A. Karbakhshzadeh, M. Derakhshande, N. Farhami, A. Hosseinian, S. Ebrahimiasl and A. Ebadi, Study the adsorption of letrozole drug on the silicon doped graphdiyne monolayer: A DFT investigation, *Silicon*, 2022, **14**(7), 3615–3622.

77 J. D. Kubicki, K. W. Paul, L. Kabalan, Q. Zhu, M. K. Mrozik, M. Aryanpour, *et al.*, ATR–FTIR and density functional theory study of the structures, energetics, and vibrational spectra of phosphate adsorbed onto goethite, *Langmuir*, 2012, **28**(41), 14573–14587.

78 A. A. Tamijani, A. Salam and M. P. de Lara-Castells, Adsorption of noble-gas atoms on the TiO2 (110) surface: An Ab initio-assisted study with van der Waals-corrected DFT, *J. Phys. Chem. C*, 2016, **120**(32), 18126–18139.

79 Z. Wei, K. Liang, Y. Wu, Y. Zou, J. Zuo, D. C. Arriagada, *et al.*, The effect of pH on the adsorption of arsenic (III) and arsenic (V) at the TiO2 anatase [1 0 1] surface, *J. Colloid Interface Sci.*, 2016, **462**, 252–259.

80 L. Yan, J. Du and C. Jing, How TiO 2 facets determine arsenic adsorption and photooxidation: spectroscopic and DFT studies, *Catal. Sci. Technol.*, 2016, **6**(7), 2419–2426.

81 H. Pan, H. Hou, J. Chen, H. Li and L. Wang, Adsorption of arsenic on iron modified attapulgite (Fe/ATP): Surface complexation model and DFT studies, *Adsorption*, 2018, **24**, 459–469.

82 L. Yan, T. Chan and C. Jing, Arsenic adsorption on hematite facets: spectroscopy and DFT study, *Environ. Sci.: Nano*, 2020, **7**(12), 3927–3939.

83 M. A. Vincent and I. H. Hillier, Accurate prediction of adsorption energies on graphene, using a dispersion-corrected semiempirical method including solvation, *J. Chem. Inf. Model.*, 2014, **54**(8), 2255–2260.

84 E. Hyde and M. Beck, Comprehensive DFT study of hydroxyl coverage on titania surfaces, *Appl. Surf. Sci.*, 2019, **498**, 143893.

85 R. Rahimi, M. Solimannejad and M. Farghadani, Adsorption of chloroquine and hydroxychloroquine as potential drugs for SARS-CoV-2 infection on BC 3 nanosheets: a DFT study, *New J. Chem.*, 2021, **45**(38), 17976–17983.

86 M. Su and Y. Cheng, Functionalization of single-wall BC2N nanotubes by using amino acid: DFT study, *Bull. Mater. Sci.*, 2021, **44**(2), 151.

87 J. S. Al-Otaibi, Y. S. Mary, Y. S. Mary, R. Thomas and R. A. Costa, DFT investigations on the interactions between pyrimidine derivatives and Ag/Au/Cu metal clusters: solvation effects and reactivity analysis, *J. Cluster Sci.*, 2023, **34**(6), 2847–2858.

88 I. V. Nechaev and A. V. Vvedenskii, Quantum chemical modeling of the adsorption of chloride ion and water molecule on group 1B metals, *Prot. Met. Phys. Chem. Surf.*, 2009, **45**, 137–146.

89 J. Liu, Y. Wang, D. Luo, Y. Zeng, S. Wen and L. Chen, DFT study of SDD and BX adsorption on sphalerite (1 1 0) surface in the absence and presence of water molecules, *Appl. Surf. Sci.*, 2018, **450**, 502–508.

90 M. Reda, H. A. Hansen and T. Vegge, DFT study of stabilization effects on N-doped graphene for ORR catalysis, *Catal. Today*, 2018, **312**, 118–125.

91 E. C. Lewis and N. Y. Dzade, First-principles density functional theory characterisation of the adsorption complexes of H3AsO3 on cobalt ferrite (Fe2CoO4) surfaces, *Minerals*, 2021, **11**(2), 195.

92 A. Malloum, K. A. Adegoke, J. O. Ighalo, J. Conradie, C. R. Ohoro, J. F. Amaku, *et al.*, Computational methods for adsorption study in wastewater treatment, *J. Mol. Liq.*, 2023, 123008.

93 X. Meng, X. Li, Q. Zhang, R. Zheng, L. Wu and F. Cao, Interfacial adsorption and electron properties of water molecule/cluster on anatase TiO2 (101) surface: Raman and DFT investigation, *Langmuir*, 2022, **38**(3), 1057–1066.

94 V. Vetrivelan, S. Sakthivel, S. Muthu and A. A. Al-Saadi, Non-covalent interaction, adsorption characteristics and solvent effect of procainamide anti-arrhythmias drug on silver and gold loaded silica surfaces: SERS spectroscopy, density functional theory and molecular docking investigations, *RSC Adv.*, 2023, **13**(14), 9539–9554.

95 J. B. Pandya, P. D. Patel, S. M. Shinde and P. K. Jha, Interpreting the nature of interactions in the inclusion complex of danofloxacin, a third-generation fluoroquinolone with Cucurbit[7]uril: A computational study, *Comput. Theor. Chem.*, 2021, **1199**, 113210.

96 A. Shahali, M. Farahmand, H. A. Hussein, M. M. Kadhim, W. K. Abdelbasset, A. G. Ebadi, *et al.*, Quantum chemical study the interaction between thiotepa drug and silicon doped graphdiyne, *Comput. Theor. Chem.*, 2022, **1209**, 113612.

97 F. Manouchehri and S. Iranpanah, Thioguanine adsorption on the γ-graphyne and its boron nitride analogue as promising drug delivery system: Electronic study via DFT, *Inorg. Chem. Commun.*, 2022, **144**, 109774.

98 M. Ishtiaq, M. U. Khan, A. Hamid, J. Yaqoob, R. Hussain and A. Ali, Systematic study of the structure-property relationship of C24N24 nanoclusters for the detection and electrochemical sensing of chemical warfare agents: molecular modelling at DFT level, *J. Mol. Struct.*, 2024, **1307**, 137905.

99 Y. Li, Y. Xu and X. Li, The sensing mechanism of HCHO gas sensor based on transition metal doped graphene: Insights from DFT study, *Sens. Actuators, A*, 2022, **338**, 113460.

100 E. D. Glendening, A. E. Reed, J. E. Carpenter and F. Weinhold, *NBO Version 3.1*. Gaussian Inc., Pittsburgh, References-Scientific Research Publishing nd, 2003.

101 R. A. Taha, A. S. Shalabi, M. M. Assem and K. A. Soliman, DFT study of adsorbing SO2, NO2, and NH3 gases based on pristine and carbon-doped Al24N24 nanocages, *J. Mol. Model.*, 2023, **29**, 140.

102 J. Panchal, A. Gauswami, D. Chodvadiya, H. Jadeja and P. K. Jha, Adsorption performance of CO, NO and NH3 hazardous gas molecules over B9N9 and Al9N9 nanorings: Acumen from density functional theory, *Mater. Chem. Phys.*, 2024, **311**, 128565.

103 H. Wang, L. Yu, J. Xu, D. Wei, G. Qin and Y. Yao, Intrinsically low lattice thermal conductivity of monolayer hexagonal aluminum nitride (h-AlN) from first-principles: a comparative study with graphene, *Int. J. Therm. Sci.*, 2021, **162**, 106772.

104 E. Hosseinzadeh, A. Foroumadi and L. Firoozpour, A DFT study on the transition metal doped BN and AlN nanocages as a drug delivery vehicle for the cladribine drug, *J. Mol. Liq.*, 2023, **374**, 121262.

105 R. Sainda, D. Chodvadiya, I. Zgłobicka, K. J. Kurzydłowski and P. K. Jha, The First-Principles investigation of sensing and removal applications of nitrobenzene using pristine and Sc decorated B9N9 nanoring, *J. Mol. Liq.*, 2024, **409**, 125389.

106 H. Sajid, K. Ayub and T. Mahmood, Sensing behaviour of monocyclic C18 and B9N9 analogues toward chemical warfare agents (CWAs); quantum chemical approach, *Surf. Interfaces*, 2022, **30**, 101912.

107 N. A. Tukadiya, S. K. Jana, B. Chakraborty and P. K. Jha, C24 Fullerene and its derivatives as a viable glucose sensor: DFT and TD-DFT studies, *Surf. Interfaces*, 2023, **41**, 103220.

108 C. Zhang and M. Derakhshandeh, CS2 adsorption on pristine and Al-doped graphynes: A DFT study, *Comput. Theor. Chem.*, 2021, **1204**, 113380.

109 H. Ji, T. Wang, T. Huang, B. Lai and W. Liu, Adsorptive removal of ciprofloxacin with different dissociated species onto titanate nanotubes, *J. Cleaner Prod.*, 2021, **278**, 123924.

110 A. M. Aljeboree, N. D. Radia, L. S. Jasim, A. A. Alwarthan, M. M. Khadhim, A. W. Salman, *et al.*, Synthesis of a new nanocomposite with the core TiO2/hydrogel: Brilliant green dye adsorption, isotherms, kinetics, and DFT studies, *J. Ind. Eng. Chem.*, 2022, **109**, 475–485.

111 Y. Du, H. Che, P. Wang, J. Chen and Y. Ao, Highly efficient removal of organic contaminant with wide concentration range by a novel self-cleaning hydrogel: Mechanism, degradation pathway and DFT calculation, *J. Hazard. Mater.*, 2022, **440**, 129738.

112 H. Wang, X. Li, J. Li, Z. Xie and G. Chang, Synthesis of a "Turn-On" Mg2+ fluorescent probe and its application in hydrogel adsorption, *J. Mol. Struct.*, 2023, **1281**, 135085.

113 L. Jayarathna, A. Bandara, W. J. Ng and R. Weerasooriya, Fluoride adsorption on γ− Fe 2 O 3 nanoparticles, *J. Environ. Health Sci. Eng.*, 2015, **13**, 1–10.

114 Q. Shi, L. Yan, T. Chan and C. Jing, Arsenic adsorption on lanthanum-impregnated activated alumina: spectroscopic and DFT study, *ACS Appl. Mater. Interfaces*, 2015, **7**(48), 26735–26741.

115 D. D. Justino, M. O. Alves, B. R. L. Galvão, R. Santamaría, F. B. De Sousa and P. F. R. Ortega, The effects of functionalization on graphene oxide for organic dye adsorption: An experimental-theoretical study using electronic structure calculations and statistical mechanical modeling, *J. Mol. Liq.*, 2023, **387**, 122612.

116 A. Molla, Y. Li, B. Mandal, S. G. Kang, S. H. Hur and J. S. Chung, Selective adsorption of organic dyes on graphene oxide: Theoretical and experimental analysis, *Appl. Surf. Sci.*, 2019, **464**, 170–177.

117 W. Xu, Y. Chen, Y. Zhao, M. Zhang, R. Tian and C. Zhang, Methane adsorption properties of N-doped graphdiyne: a first-principles study, *Struct. Chem.*, 2021, **32**, 1517–1527.

118 Z. Tabandeh and A. Reisi-Vanani, Investigation of the adsorption behavior of two anticancer drugs on the pristine and BN-doped graphdiyne nanosheet: A DFT-D3 perception, *Diamond Relat. Mater.*, 2021, **119**, 108564.

119 H. Sajid, S. Khan, K. Ayub and T. Mahmood, Effective adsorption of A-series chemical warfare agents on graphdiyne nanoflake: a DFT study, *J. Mol. Model.*, 2021, **27**, 117.

120 A. Karbakhshzadeh, M. Derakhshande, N. Farhami, A. Hosseinian, S. Ebrahimiasl and A. Ebadi, Study the Adsorption of Letrozole Drug on the Silicon Doped Graphdiyne Monolayer: a DFT Investigation, *Silicon*, 2022, **14**, 3615–3622.

121 A. Kanzariya, S. Vadalkar, S. K. Jana, L. K. Saini and P. K. Jha, An ab-initio investigation of transition metal-doped graphene quantum dots for the adsorption of hazardous CO2, H2S, HCN, and CNCl molecules, *J. Phys. Chem. Solids*, 2024, **186**, 111799.